[Geophysical Research Letters]

Supporting Information for

Direct observation of shock-induced disordering of enstatite below the melting temperature

J.-A. Hernandez[1,2], G. Morard[3,4], M. Guarguaglini[1], R. Alonso-Mori[5], A. Benuzzi-Mounaix[1], R. Bolis[1], G. Fiquet[3], E. Galtier[5], A. E. Gleason[5], S. Glenzer[5], F. Guyot[3], B. Ko[7], H. J. Lee[5], W. L. Mao[6], B. Nagler[5], N. Ozaki[8,9], A. K. Schuster[10,11], S. H. Shim[7], T. Vinci[1], and A. Ravasio[1]

[1]Laboratoire pour l'Utilisation des Lasers Intenses (LULI), Ecole Polytechnique, CNRS, CEA, UPMC, 91128 Palaiseau, France

[2]Centre for Earth Evolution and Dynamics, University of Oslo, Norway

[3]Sorbonne Université, Institut de Minéralogie, de Physique des Matériaux et de Cosmochimie, IMPMC, UMR CNRS 7590, Museum National d'Histoire Naturelle, IRD, 4 Place Jussieu, 75005 Paris, France

[4]Institut des Sciences de la Terre, Université Grenoble-Alpes, 1381 rue de la Piscine, 38610 Gières, France

[5]SLAC National Accelerator Laboratory, 2575 Sand Hill Rd., Menlo Park, CA 94025, USA

[6]Stanford Institute for Materials and Energy Sciences, SLAC National Accelerator Laboratory, 2575 Sand Hill Rd., Menlo Park, CA 94025, USA

[7]School of Earth and Space Exploration, Arizona State University, Tempe, Arizona, USA

[8]Graduate School of Engineering, Osaka University, Suita, Osaka 565-0871, Japan

[9]Institute of Laser Engineering, Osaka University, Suita, Osaka 5650871, Japan

[10]Helmholtz-Zentrum Dresden-Rossendorf, Bautzner Landstr. 400, D-01328 Dresden, Germany

[11]Institute of Solid State and Materials Physics, Technische Universität Dresden, 01069 Dresden, Germany

Contents of this file

S1. EXPERIMENTAL SETUP

Figure S1 presents the experimental configuration used at LCLS MEC end-station and the target designs.

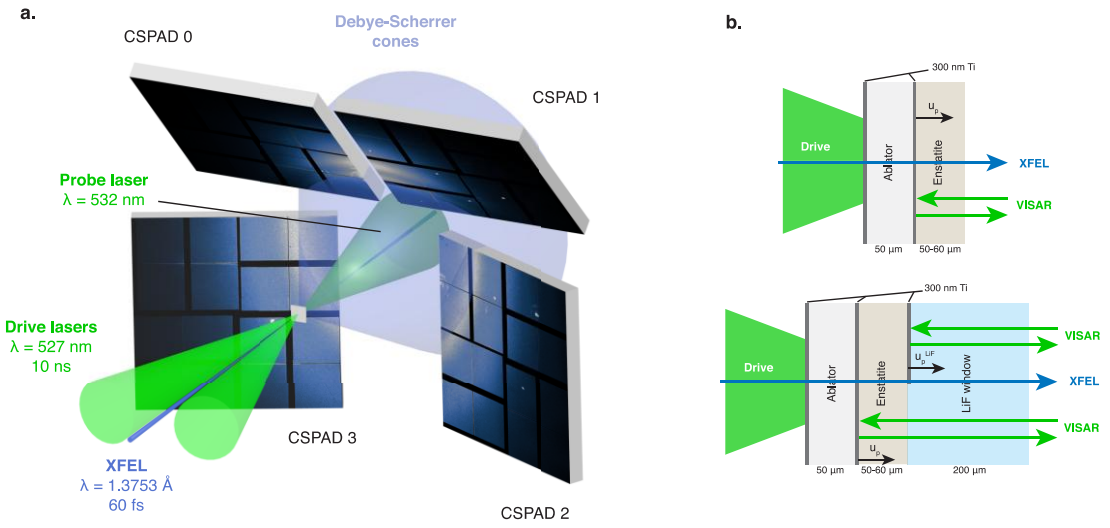

Figure S1: Experimental configuration and orthoenstatite target design. **a.** The structure of laser-shocked enstatite was sampled under quasi-uniform pressure conditions and quasi-instantaneously using the 60 fs XFEL beam. The diffracted rays were collected in transmission geometry on four CSPADs positioned around the XFEL axis. **b.** Two types of multi-layered targets were used to check the shock steadiness. The interaction between the drive laser and the polystyrene (PS) ablator generates a shock wave that propagates in the sample. Shock and particle velocities were measured by interferometry (VISAR) using a probe laser.

Enstatite samples come from two enstatite gem quality single crystals from Mogok (Myanmar) that have been characterized by single crystal XRD using an Xcalibur Sapphire3 diffractometer. Their structures were solved and refined using ShelXT and ShelXL programs (Sheldrick et al. 2015a, 2015b) considering a unique substitution between Mg and Fe. We obtained densities of 3.219±0.011 g.cm^{-3} and 3.259±0.011 g.cm^{-3} for the two crystals and $Mg_{0.98}Fe_{0.02}SiO_3$ and $Mg_{0.93}Fe_{0.07}SiO_3$ as respective compositions. The majority of the targets did not include the LiF window and the determination of $MgSiO_3$ fluid and shock velocities was done as described in the main text. For targets with LiF windows, the VISAR measured the

apparent velocity of the enstatite/LiF interface (U_{app}^{LiF}) by reflection of the probe laser on the thin Ti coating. The particle velocity in the LiF window (U_p^{LiF}) was obtained from U_{app}^{LiF} from the relation $U_p^{LiF} = 0.7827 U_{app}^{LiF\ 0.9902}$ (Rigg et al. 2014). Then the fluid velocity in enstatite (U_p) was deduced by impedance matching between enstatite and LiF considering the LiF Hugoniot relation $U_s^{LiF} = 5.215 + 1.351 U_p^{LiF}$ and a density of 2.640 $g.cm^{-3}$ for unshocked LiF as in Rigg et al. (2014), and using the mirror Hugoniot of enstatite to describe its release. The mean shock velocity in enstatite (U_s) was obtained from the time difference between the shock entrance in the enstatite and the shock entrance in the LiF window. The subsequent independent U_p-U_s measurements (Figure S2) are in agreement with the linear relation found in the literature (Luo et al. 2004, Akins et al. 2004, Fratanduono et al. 2018).

S2. SAMPLED CONDITIONS

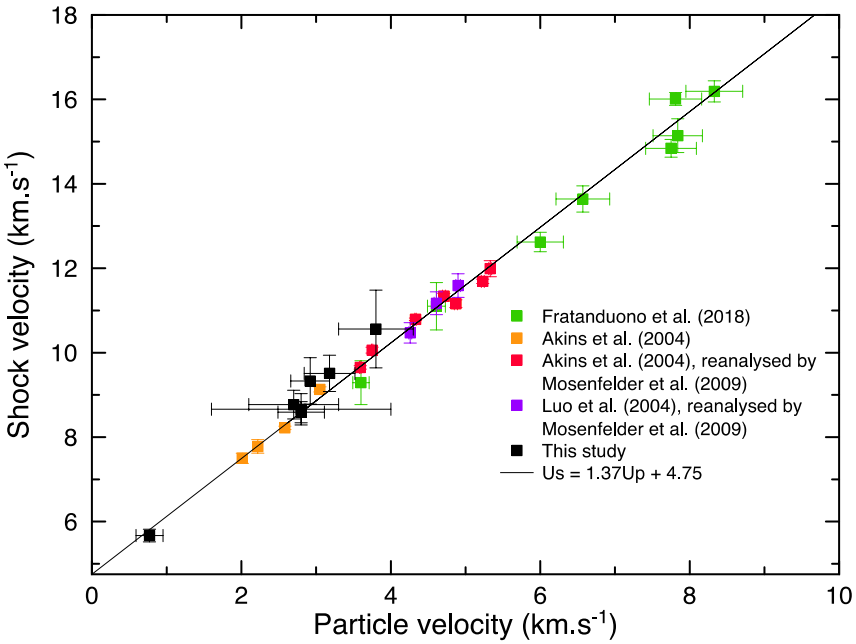

Figure S2: Comparison of the sampled conditions with existing measurements along the principal Hugoniot of $MgSiO_3$ orthoenstatite. In this plot, we only show our data points for which both the shock velocity and the particle velocity were measured during the shock (see Table S1). For the other shots, when only one velocity was measured, we estimated the missing one using the linear relation constructed by Frantanduono et al. (2018).

Table S1: Velocity measurements and thermodynamic conditions achieved in shocked orthoenstatite. Values in italic have been calculated using the linear relation $U_S = 1.37(\pm0.01)U_P + 4.75(\pm0.03)$ from Fratanduono et al. (2018). Up values underlined have been determined using for Up^{LiF} and impedance matching. t_{XRD}-t_0 and t_{BO}-t_{XRD} respectively corresponds to the delay between the shock entrance in the sample and the XRD, and between the XRD and the shock break out. Errors on the last decimal are given between parenthesis and have been estimated using a Monte-Carlo procedure taking into account errors on the target thickness, timings, VISAR phase shift, and on the effective refractive index of enstatite. The shots presented in the second part of the table were performed without phase plate.

Shot #	ρ_0 ($g.cm^{-3}$)	Us ($km.s^{-1}$)	Up ($km.s^{-1}$)	P_{VISAR} (GPa)	ρ_{VISAR} ($g.cm^{-3}$)	t_{XRD}-t_0 (ns)	t_{BO}-t_{XRD} (ns)	Structure from XRD
102	3.219(11)	5.67(18)	<u>0.77(18)</u>	14(3)	3.725(139)	5.9	4.5	En. + dense pyroxenoid
83	3.259(11)	8.66(37)	2.8(9)	79(26)	4.816(746)	0.3	6.2	En. only
84	3.259(11)	*8.51(16)*	<u>2.75(11)</u>	76(3)	4.815(103)	< 1ns		En. + dense pyroxenoid
82	3.219(11)	8.77(34)	2.7(6)	76(17)	4.651(467)	3.8	2.7	En. + dense pyroxenoid
88	3.259(11)	9.33(55)	2.92(26)	89(10)	4.744(231)	5.5	0.5	En. + dense pyroxenoid + disordered (faint)
81	3.219(11)	9.51(43)	3.18(34)	97(11)	4.836(283)	6.5	-0.4	En. + dense pyroxenoid + disordered
87	3.259(11)	10.09(45)	*3.90(33)*	128(18)	5.311(138)	4.9	0.55	En. + dense pyroxenoid + disordered
79	3.219(11)	10.56(92)	3.8(5)	129(20)	5.028(446)	5.3	0.1	Disordered
90	3.259(11)	10.88(86)	*4.47(63)*	159(35)	5.532(147)	4.4	1.3	Disordered
210	3.259(11)	8.59(25)	2.80(31)	78(7)	4.835(268)	1.9	4.5	En. + dense pyroxenoid
212	3.259(11)	8.64(42)	*2.84(35)*	80(13)	4.855(145)	1.7	4.9	En. + dense pyroxenoid + disordered
209	3.259(11)	10.36(62)	*4.10(46)*	138(24)	5.393(183)	2.8	2.7	Disordered
208	3.259(11)	10.59(47)	*4.26(35)*	147(19)	5.452(139)	1.6	3.5	Disordered
106	3.259(11)	11.37(86)	*4.83(63)*	179(37)	5.666(230)	3.7	1.4	Disordered
110	3.259(11)	14.50(95)	*7.12(70)*	337(55)	6.403(205)	4	0	Disordered (above melting line)
107	3.259(11)	13.85(83)	*6.64(61)*	300(46)	6.260(188)	3.6	0.3	Disordered (above melting line)
206	3.259(11)	14.19(102)	*6.89(74)*	319(57)	6.335(222)	4.6	-0.3	Disordered (above melting line)

S3. AZIMUTHAL INTEGRATION OF THE DIFFUSE SIGNAL FROM STRUCTURALLY DISORDERED $MgSiO_3$

Azimuthal integration of XRD images presenting amorphous features was done separately for each CSPAD using the following procedure. Dark patterns were subtracted from all XRD images. No significant contribution to shock sample patterns was observed from the ablator material as the shocked ablator signal has an extremely low intensity. We masked the spots either coming from the unshocked enstatite volume or from the shocked single crystal when it coexists with the amorphous signal (e.g. at 128±18 GPa). To remove any discontinuity in the integrated spectra due to the gaps between CSPAD's individual units, we projected the image in the (2θ,ϕ) plane and interpolated intensities as a function of the azimuthal angle (ϕ) for each 2θ-angle (Figure S3). Azimuthal integration was then performed in a continuous (2θ,ϕ) region with the pyFAI library (Ashiotis et al. 2015).

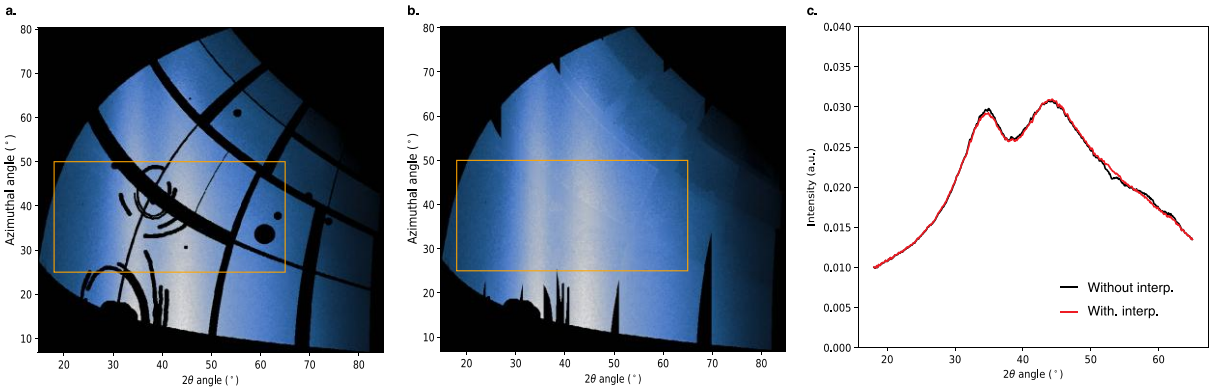

Figure S3: Azimuthal integration of XRD diffuse signal from the disordered structure. a. XRD image projected on the scattering angle (2θ) – azimuthal angle (ϕ) plane after the diffraction spots coming from the unshocked and shocked part of the target have been masked. The orange rectangle delimits the integration zone. b. XRD image after interpolation of the masked regions based on 3rd order polynomial fitting of the intensities I = f(ϕ) at given 2θ-angle and addition of a noise similar to the one of the unmasked regions. c. Spectra resulting from the azimuthal integration without or with interpolation (interp.) of the masked regions. The interpolation slightly smoothens the final spectra.

S4. CRYSTALLINE STRUCTURES OBSERVED BETWEEN 14(3) AND 78(7) GPa

We best reproduce the positions of the diffraction spots in the data considering three different pyroxenoids: (i) the unshocked orthoenstatite sampled along [100]; (ii) compressed orthoenstatite

sampled along [100]; (iii) metastable β-post-orthopyroxene (β-popx) oriented along [001], as observed and described in Finkelstein et al. (2015) from static compression of single crystal orthopyroxenes up to 48.5 GPa at 300 K. Finkelstein et al. (2015) suggest that β-popx can be maintained up to at least 70 GPa based on earlier Raman spectroscopy measurement (Serghiou et al. 2000).

We point out that the unit-cell parameter *a* of enstatite (and respectively *c* of β-popx) are poorly constrained as they have a small influence on the position of the diffraction spots in the collected range of scattering angles as they are aligned with the direction of the XFEL probe. This last geometrical constraint, combined to the width of the diffraction spots precludes further detailed structure refinement – making the distinction between all structurally close pyroxene- and post-pyroxene-like structures difficult (e.g. Jahn et al. 2008, Zhang et al. 2012, Finkelstein et al. 2015), and prevents accurate density estimation from the XRD.

Compressed enstatite and β-popx seem to form at different times as shown by three diffraction images obtained at the same pressure conditions (76±3, 76±17 and 79±26 GPa) but at different pump-probe delays (see Figure S4). A few hundred of picoseconds after the shock enters in the sample, only compressed enstatite is detected. The signal from the β-popx emerges within less than 1 ns, and is predominant at 3.8 ns.

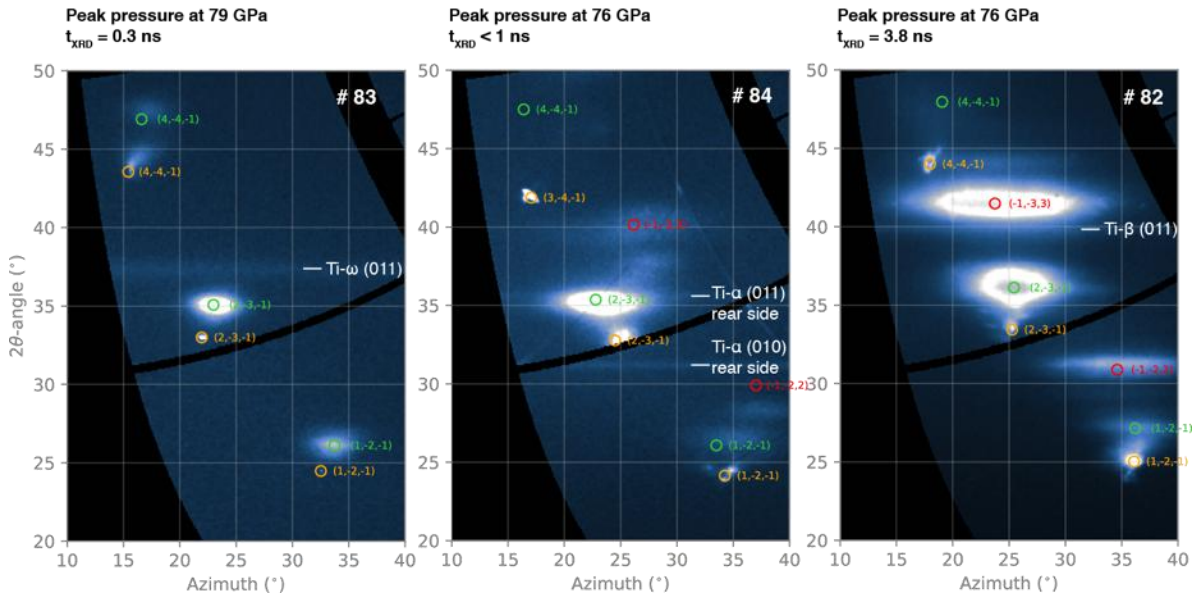

Figure S4: Time evolution of the diffracted signal at 76-79 GPa. In shots #83, #84 and #82, crystalline orthoenstatite has been shocked at similar conditions but probed at different times after shocked entrance in the sample (t_{XRD}). Diffraction spots from the unshocked part of the sample appear on all three images; orange circles show the expected positions of the corresponding (hkl) planes

(orange labels) for ambient conditions orthoenstatite. At t_{XRD} = 0.3 ns, an additional set of spots is visible that we attribute to compressed orthoenstatite (green circles and labels) with $a \sim 0.960*a_0$, $b \sim 0.935*b_0$ and $c \sim 0.930*c_0$ with a_0 = 18.2330 Å, b_0 = 8.8191 Å, c_0 = 5.1802 Å, the unit-cell parameter of unshocked orthoenstatite. This corresponds to a density of ~3.84 g.cm^{-3}. A few hundred picoseconds later, several sets of new diffraction spots arise in addition to the ones from the still visible compressed enstatite. Among these new spots, only the one at the highest 2θ-angle remains at 3.8 ns. For shots #84 and #82, they are best matched considering β-popx (red circles and labels) with $a \sim 0.82*c_0$, $b \sim 0.83*b_0$ and $c \sim 0.94*a_0$. This corresponds to a density of ~5.00 g.cm^{-3} for β-popx, slightly larger than the density deduced from the VISAR data at the same pressure.

S5. SIMULATION OF POWDER DIFFRACTION PATTERNS

We simulated powder XRD patterns of Bd and Ppv at 4.836 g.cm^{-3} and 5.532 g.cm^{-3} respectively with a grain size of 3 nm (see Figure S5) using the Python library *X-ray utilities* (Kriegner et al. 2013) and using the equations of state from Fiquet et al. (1998) for Bd and from Guignot et al. (2007) for Ppv.

From a given structure we computed the structure factor (S) using the atomic scattering factors from the ESRF XOP DABAX database (http://ftp.esrf.eu/pub/scisoft/xop2.3/DabaxFiles/). The line intensities (I) are obtained from the structure factor ($I(q) = |S(q)|^2$) and are eventually corrected for polarization effects.

X-ray utilities employs the formalism described in Mendenhall et al. (2015) to model the diffraction line profiles. In particular, the effect of the crystallite size is taken into account based on the Scherrer relation $B(2\theta) = K\lambda/(L\cos(2\theta))$ where B is the full width at half maximum of the diffraction peak, L is the characteristic size of the crystallites, λ the wavelength of the X-ray source and K a proportionality constant set to 1. The Gaussian profile associated to the grain size is convoluted to an instrument profile function (itself resulting from the convolution of a geometric profile and of a given emission spectrum). The convolution of the resulting profile with the powder diffraction lines, and the mapping onto the 2θ-angle positions gives the final XRD spectrum. In this study, we used *X-ray utilities* default parameters to define the instrument profile considering a monochromatic source at λ = 1.3753 Å as the peak broadening induced by nanometer-sized grains largely overlaps other possible instrumental effects in our case.

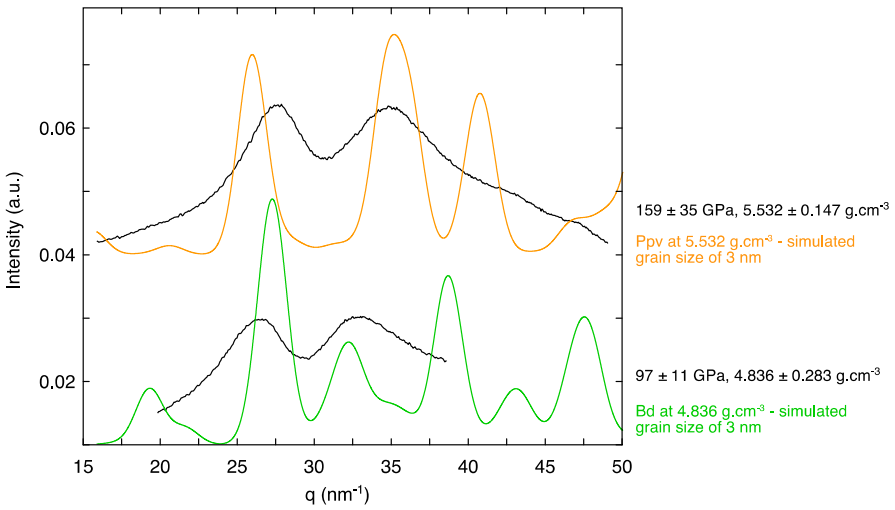

Figure S5: Comparison of the XRD spectra of the disordered component formed during shock compression of enstatite (black) with simulated spectra of bridgmanite (green) and post-perovskite (orange) powders with a grain size of 3 nm and at comparable densities.

S6. OPTICAL PROPERTIES OF DISORDERED $MgSiO_3$

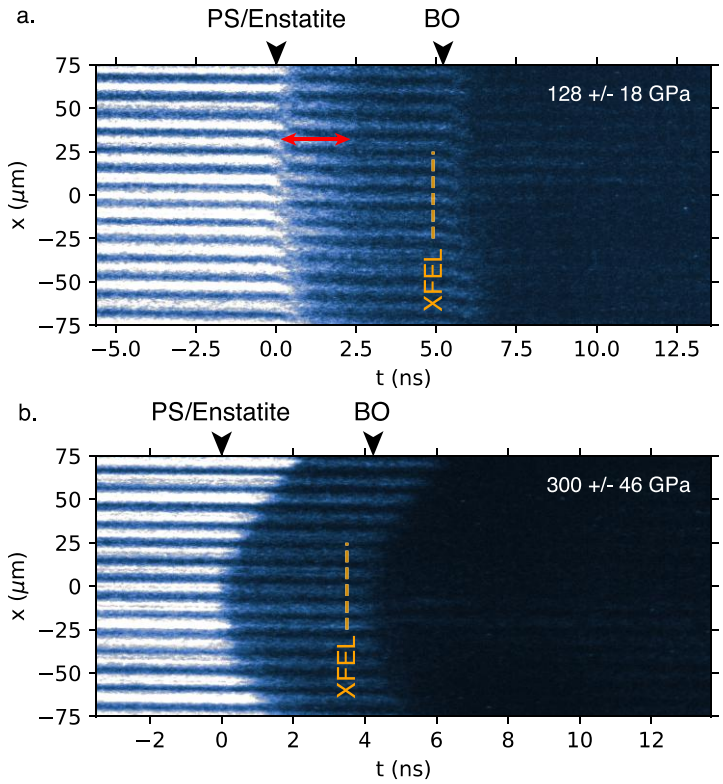

Figure S6: VISAR images corresponding to the XRD data of Figure 2 and showing a large absorption depth at 128±18 GPa (**a.**) and an opaque (or weakly reflecting) state at 300±46 GPa as expected for the equilibrium metallic melt (**b.**). Black arrows show the position of the shock entrance in the enstatite sample and the position of the shock breakout (BO) at x = 0. In panel **a.**, the red arrow indicates the time interval during which the probe laser still reflects on the PS/Enstatite interface. Within this interval, the reflectivity shows a characteristic exponential decay prior reaching a plateau corresponding to parasite reflections ("ghost fringes") that persist at latter time up to the shock breakout. By converting this time interval, during which enstatite is still transparent, into the corresponding thickness of compressed enstatite, and fitting a Beer-Lambert law, we find an absorption length of 17.4±0.4 μm at a wavelength of 532 nm. In panel b., only ghost fringes are visible during the shock transit into the sample, indicating that shocked enstatite is opaque or weakly reflecting at 300 ± 46 GPa.

S7. TIME EVOLUTION OF SiO_2 AND $MgSiO_3$ HUGONIOTS

In the following, we argue that Bd or Ppv may crystallize at microsecond-scale in gas gun experiments. This interpretation is based on the temperature difference between the Hugoniot of the disorder state (glass or liquid) and the Hugoniot of Ppv.

Fratanduono et al. (2018) have measured the temperature of laser-shocked enstatite in the liquid domain (above 227 GPa). This measurement is in very good agreement with the Hugoniot of liquid $MgSiO_3$ predicted by DFT-MD using both the GGA (Militzer 2013) and LDA functionals (Millot et al. 2020). Moreover, these predictions show that for a given functional the Hugoniot of dense $MgSiO_3$ glass (e.g. De Koker and Stixrude 2009) corresponds to the extension of the liquid state Hugoniot (e.g. Millot et al. 2020) below the melting line as there is no drastic density and internal energy change at the glass/liquid transition (see Figure 4 of the main text).

Our *in situ* XRD measurements in shocked enstatite show that a disordered state (either glass or liquid) forms at nanosecond-scale above 80 GPa with a similar structure as expected from atomistic simulations of dense $MgSiO_3$ glass/liquid (Ghosh et al. 2014, Morard et al. 2020). Therefore, we estimate the temperature of the shots above 80 GPa based on the aforementioned Hugoniot curves of dense $MgSiO_3$ glass and liquid.

At a given pressure, the temperatures measured in gas gun shocked enstatite (for shots between 142 and 181 GPa, Luo et al. 2004) are more than 1000 K higher than the temperatures of the disordered state Hugoniot, and are in excellent agreement with the Hugoniot of Ppv predicted by DFT-MD using the GGA functional (Militzer 2013). This suggests that, between 80 GPa and the melting line, shocked enstatite first collapses into a disordered state at nanosecond-scale and then crystallizes into Bd or Ppv at microsecond-scale, which increases the temperature as latent heat is released.

Such behavior has already been modelled in shocked fused silica and shocked α-quartz (Shen et al. 2016a, 2016b) where homogeneous crystallization of stishovite occurs much faster, within few nanoseconds as measured by *in situ* XRD (Gleason et al. 2015). According to Shen et al. (2016a, 2016b), the transient disordered state lasts only few hundred picoseconds before stishovite grains start to nucleate and growth. This fast crystallization kinetics of stishovite below the melting line explain the good agreement between laser-driven (nanosecond-scale; Hicks et al. 2006, Gleason

et al. 2015, Millot et al. 2015) and gas gun (microsecond-scale; Sugiura et al. 1982, Lyzenga et al. 1983) Hugoniot measurements in silica.

The time-dependence of SiO_2 and $MgSiO_3$ Hugoniot paths is illustrated in Figure S7.

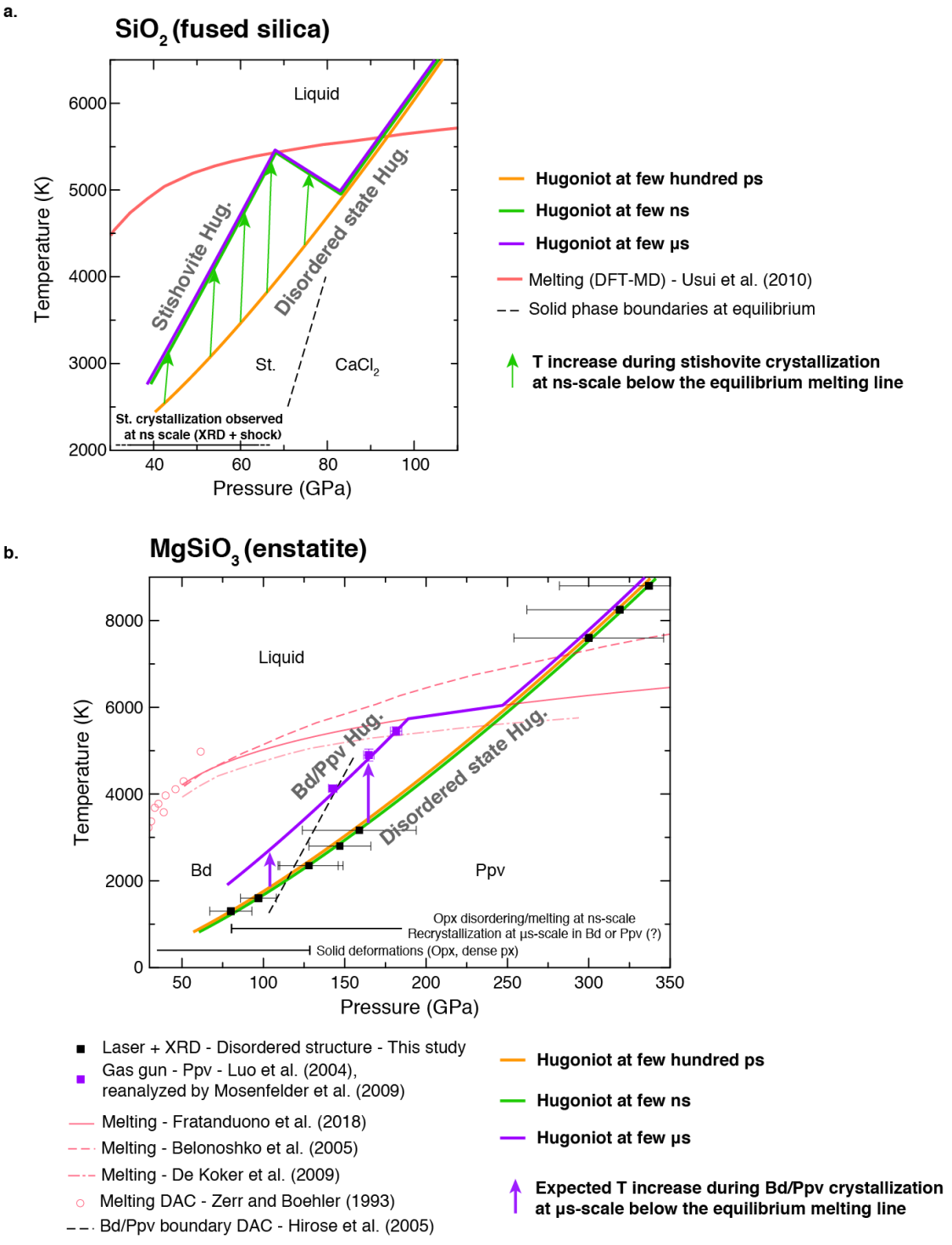

Figure S7: a. Evolution of shocked fused-SiO_2 Hugoniot as function of the peak pressure duration based on both experimental data (Sugiura et al. 1982, Lyzenga et al. 1983, Hicks et al. 2006, Millot et al. 2015, Gleason et al. 2015, Tracy et al. 2018) and atomistic simulations of the shock compression (Shen et al. 2016a, 2016b). The black horizontal bar lying above the top x-axis indicates the range of pressures where polycrystalline stishovite has been detected by *in situ* XRD in shock-compressed fused silica in a laser experiment (Gleason et al. 2015) and in a gas-gun experiment (Tracy et al. 2018). **b.** Evolution of shocked $MgSiO_3$ enstatite Hugoniot as function of the peak pressure duration. Within few nanoseconds, enstatite collapses into a disordered state from which Bd or Ppv are expected to crystallize at microsecond scale. See text for more details.

ADDITIONAL REFERENCES

Fiquet, G., Andrault, D., Dewaele, A., Charpin, T., Kunz, M., & Haüsermann, D. (1998). PVT equation of state of MgSiO3 perovskite. *Physics of the Earth and Planetary Interiors*, *105*(1), 21-32.

Fratanduono, D. E., Millot, M., Kraus, R. G., Spaulding, D. K., Collins, G. W., Celliers, P. M., & Eggert, J. H. (2018). Thermodynamic properties of MgSiO 3 at super-Earth mantle conditions. *Physical Review B*, *97*(21), 214105.

Gleason, A. E., Bolme, C. A., Lee, H. J., Nagler, B., Galtier, E., Milathianaki, D., ... & Collins, G. W. (2015). Ultrafast visualization of crystallization and grain growth in shock-compressed SiO2. *Nature communications*, *6*(1), 1-7.

Guignot, N., Andrault, D., Morard, G., Bolfan-Casanova, N., & Mezouar, M. (2007). Thermoelastic properties of post-perovskite phase MgSiO3 determined experimentally at core–mantle boundary P–T conditions. *Earth and Planetary Science Letters*, *256*(1-2), 162-168.

Hicks, D. G., Boehly, T. R., Eggert, J. H., Miller, J. E., Celliers, P. M., & Collins, G. W. (2006). Dissociation of liquid silica at high pressures and temperatures. *Physical Review Letters*, *97*(2), 025502.

Kriegner, D., Wintersberger, E., & Stangl, J. (2013). xrayutilities: a versatile tool for reciprocal space conversion of scattering data recorded with linear and area detectors. *Journal of applied crystallography*, *46*(4), 1162-1170.

Lyzenga, G. A., Ahrens, T. J., & Mitchell, A. C. (1983). Shock temperatures of SiO2 and their geophysical implications. *Journal of Geophysical Research: Solid Earth*, *88*(B3), 2431-2444.

Mendenhall, M. H., Mullen, K., & Cline, J. P. (2015). An implementation of the Fundamental Parameters Approach for analysis of X-ray powder diffraction line profiles. *Journal of research of the National Institute of Standards and Technology*, *120*, 223.

Millot, M., Dubrovinskaia, N., Černok, A., Blaha, S., Dubrovinsky, L., Braun, D. G., ... & Jeanloz, R. (2015). Shock compression of stishovite and melting of silica at planetary interior conditions. *Science*, *347*(6220), 418-420.

Rigg, P. A., Knudson, M. D., Scharff, R. J., & Hixson, R. S. (2014). Determining the refractive index of shocked [100] lithium fluoride to the limit of transmissibility. *Journal of Applied Physics*, *116*(3), 033515.

Shen, Y., Jester, S. B., Qi, T., & Reed, E. J. (2016). Nanosecond homogeneous nucleation and crystal growth in shock-compressed SiO2. *Nature materials*, *15*(1), 60-65.

Shieldrick, G. M. (2015). SHELXT – Integrated space-group and crystal-structure determination. Acta Crystallographica A, 71, 3-8.

Shieldrick, G. M. (2015). Crystal structure refinement with *SHELXL*. Acta Crystallographica C, 71, 3-8.

Sugiura, H., Kondo, K., & Sawaoka, A. (1982). Shock temperatures in fused silica measured by optical technique. *Journal of Applied Physics*, *53*(6), 4512-4514.

Tracy, S. J., Turneaure, S. J., & Duffy, T. S. (2018). In situ x-Ray diffraction of shock-compressed fused silica. *Physical review letters*, *120*(13), 135702.